

# Accurate Gaussian Process Distance Fields with applications to Echolocation and Mapping

Cedric Le Gentil<sup>1</sup>, Othmane-Latif Ouabi<sup>2,3</sup>, Lan Wu<sup>1</sup>, Cedric Pradalier<sup>3</sup> and Teresa Vidal-Calleja<sup>1</sup>

**Abstract**—This paper introduces a novel method to estimate distance fields from noisy point clouds using Gaussian Process (GP) regression. Distance fields, or distance functions, gained popularity for applications like point cloud registration, odometry, SLAM, path planning, shape reconstruction, etc. A distance field provides a continuous representation of the scene. It is defined as the shortest distance from any query point and the closest surface. The key concept of the proposed method is a *reverting* function used to turn a GP-inferred occupancy field into an accurate distance field. The reverting function is specific to the chosen GP kernel. This paper provides the theoretical derivation of the proposed method and its relationship to existing techniques. The improved accuracy compared with existing distance fields is demonstrated with simulated experiments. The level of accuracy of the proposed approach enables novel applications that rely on precise distance estimation. This work presents echolocation and mapping frameworks for ultrasonic-guided wave sensing in metallic structures. These methods leverage the proposed distance field with a physics-based measurement model accounting for the propagation of the ultrasonic waves in the material. Real-world experiments are conducted to demonstrate the soundness of these frameworks.

## I. INTRODUCTION

Robotic perception and map representations are the key components of any autonomous system operating in the real world. There exist many representations to model the environment in which a system is running, each with its own specific set of applications. For example, sparse geometric features are traditionally used for Visual Odometry (VO) and Simultaneous Localisation And Mapping (SLAM) [1], [2], occupancy grids [3] allow for dense mapping and path planning [4], [5], etc. In this paper, we introduce an accurate continuous distance field representation based on Gaussian Process (GP) regression that accommodates for a wide variety of applications such as localisation, mapping, and planning.

A distance field (or distance function) is a function over a given space  $\mathbb{R}^N$  that maps a query point  $\mathbf{x}$  with the distance  $d$  to the nearest object/surface. For some regular-shaped objects, the surface can be represented with a *parametric* or *implicit* function that equals zero on the surface. The knowledge of such a function (e.g.,  $ax + by + cz + w = 0$  for

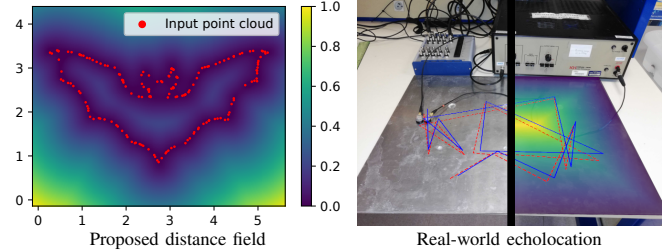


Fig. 1. Illustration of the proposed continuous GP-based distance field using noisy point clouds as input (left). The high level of accuracy allows for applications such as echolocation as shown in the right image (real-world experimental setup with an ultrasonic emitter-receiver: ground truth trajectory in blue, estimated trajectory in dashed red, and overlay of the GP-based distance field on the right half).

an infinite plane) may lead to a closed-form expression of the distance field. In the general case, the surface function and the distance field are not explicitly known and in the context of robotics, surfaces are often represented with discrete samples in the form of noisy point clouds. Distance-field-based frameworks have increased in popularity over the past decade. Using a truncated distance function, KinectFusion [6] performs dense 3D reconstruction using an RGB-D camera. Euclidean Signed Distance Fields (ESDFs) [7] allowed for novel mapping and planning methods [8], [9], [10]. More recently, leveraging the computational power of GPUs, neural-network-based representations also exploit distance fields. Several works build upon such representations for the purpose of SLAM [11], [12] and path planning [13], [14].

GP regression is a non-parametric, probabilistic interpolation method widely used for representing the environment. In [15], surface reconstruction is performed with Gaussian Process Implicit Surfaces (GPISs) modelling the world as a continuous scalar field representing the signed distance to the surface close to the object. Unfortunately, this representation does not allow for path planning/obstacle avoidance as the field converges to zero away from the surface. In [16], the LogGPIS is introduced to remedy this issue by defining a distance field over the full space. It has been shown that LogGPIS is suitable for applications like odometry, mapping, path planning, and surface reconstruction [17]. These applications rely on the fact that the distance field is minimal on the surface (e.g., distance minimisation for scan registration), and maximal the furthest away from the surface (e.g., distance maximisation for obstacle avoidance). However, LogGPIS does not provide a truly Euclidean distance field (c.f. next section) and suffers from a trade-off between

Cedric Le Gentil and Teresa Vidal-Calleja are supported by the Australian Research Council Discovery Project under Grant DP210101336. This work has been partially funded by the BugWright2 project, supported by the European Commission under grant agreement 871260 - BugWright2.

<sup>1</sup>Robotics Institute at the University of Technology Sydney, Australia {cedric.legentil; lan.wu-2; teresa.vidalcalleja}@uts.edu.au

<sup>2</sup>Sysnav, France othmane.ouabi@sysnav.fr

<sup>3</sup>International Research Lab 2958 Georgia Tech-CNRS, France cedricp@georgiatech-metz.fr

accuracy and interpolation abilities [18]. These are limiting factors for specific applications that require accurate values of the Euclidean distance field such as echolocation. The proposed method is based on the continuous representation of the  $\mathbb{R}^N$  space occupancy with a GP similarly to [19]. Given this occupancy field, we use a *reverting function* to obtain an accurate distance field allowing for echolocation as depicted in Fig. 1.

Localisation and mapping based on range measurements is an active field of study. It finds a wide range of applications such as acoustic room geometry reconstruction [20], [21], underwater localisation and mapping [22], [23], and robotic inspection [24], [25]. Yet, recent works often rely on strong assumptions on the map. For example, in [20], [21], [25] the map is modelled with a fixed set of lines, preventing the possibility to capture richer information on the environment. GP-based distance fields are appealing in this type of application as they can represent complex environments with non-parametric models. The accuracy of the distance estimates of the proposed approach enables us to tackle the problems of echolocation and mapping based on Ultrasonic Guided Waves (UGWs).

To summarise, the contributions outlined in this work further the abilities of GP regression through the derivation of a novel GP-based distance field using point clouds as input, the thorough evaluation of the proposed distance field, and its integration into echolocation and mapping frameworks using UGWs.

## II. BACKGROUND

The design of the proposed distance field heavily relies on GP regression. Accordingly, this section provides the required preliminary knowledge and explores existing distance field methods and their limits.

### A. Gaussian Process regression

GP regression is a probabilistic non-parametric method for interpolation. Let us consider an unknown signal  $h(\mathbf{x}) \in \mathbb{R}$  with  $\mathbf{x} \in \mathbb{R}^m$ , and  $Q$  noisy observations  $y_i$  defined as

$$y_i = h(\mathbf{x}_i) + \eta_i, \quad \text{where } \eta_i \sim \mathcal{N}(0, \sigma_y^2). \quad (1)$$

where  $i = (1, \dots, Q)$ . The goal is to infer the distribution (mean and variance) of  $h$  for any given input  $\mathbf{x}$ .

By modelling the signal  $h$  as a GP  $h \sim \mathcal{GP}(0, k_h(\mathbf{x}, \mathbf{x}'))$ , with  $k_h$  the covariance kernel function  $k_h(\mathbf{x}, \mathbf{x}') = \text{cov}(h(\mathbf{x}), h(\mathbf{x}'))$ , one can express occurrences of  $h$  as a multivariate Gaussian distribution

$$\begin{bmatrix} \mathbf{y} \\ h(\mathbf{x}^*) \end{bmatrix} = \mathcal{N}\left(0, \begin{bmatrix} \mathbf{K}_h(\mathbf{X}, \mathbf{X}) + \sigma_y^2 \mathbf{I} & \mathbf{k}_h(\mathbf{x}^*, \mathbf{X}) \\ \mathbf{k}_h(\mathbf{x}^*, \mathbf{X}) & k_h(\mathbf{x}^*, \mathbf{x}^*) \end{bmatrix}\right), \quad (2)$$

where  $\mathbf{y} = [y_1, \dots, y_Q]^\top$ ,  $\mathbf{x}^*$  is a query point,  $\mathbf{k}_h(\mathbf{x}^*, \mathbf{X}) = [k_h(\mathbf{x}^*, \mathbf{x}_1), \dots, k_h(\mathbf{x}^*, \mathbf{x}_Q)]$ , and  $\mathbf{K}_h(\mathbf{X}, \mathbf{X}) = [\mathbf{k}_h(\mathbf{x}_1, \mathbf{X})^\top, \dots, \mathbf{k}_h(\mathbf{x}_Q, \mathbf{X})^\top]$ . By

conditioning (2) with respect to the noisy observations, the mean and variance of  $h(\mathbf{x}^*)$  are respectively computed as

$$\hat{h}(\mathbf{x}^*) = \mathbf{k}_h(\mathbf{x}^*, \mathbf{X}) (\mathbf{K}_h(\mathbf{X}, \mathbf{X}) + \sigma_y^2 \mathbf{I})^{-1} \mathbf{y}, \quad (3)$$

$$\text{var}(h(\mathbf{x}^*)) = k_h(\mathbf{x}^*, \mathbf{x}^*) - \quad (4)$$

$$\mathbf{k}_h(\mathbf{x}^*, \mathbf{X}) (\mathbf{K}_h(\mathbf{X}, \mathbf{X}) + \sigma_y^2 \mathbf{I})^{-1} \mathbf{k}_h(\mathbf{x}^*, \mathbf{X})^\top.$$

### B. Distance fields

Considering a surface  $\mathcal{S}$  in Euclidean space  $\mathbb{R}^m$ , let us define the distance field  $d(\mathbf{x})$  with  $\mathbf{x} \in \mathbb{R}^m$  as a scalar-valued continuous function that represents the shortest distance between the input  $\mathbf{x}$  and the surface  $\mathcal{S}$ . Such a function is a solution to the Eikonal equation

$$|\nabla d(\mathbf{x})| = 1 \quad \text{with} \quad d(\mathbf{x}) = 0 \iff \mathbf{x} \in \mathcal{S}. \quad (5)$$

Unfortunately, as per its non-linear nature, (5) does not possess a known general closed-form solution. The aim of this work is to estimate the Euclidean distance  $\hat{d}$  given a finite set of points on the surface  $\mathbf{x}_i \in \mathcal{S}$  with  $i = (1, \dots, Q)$ . Implicitly, this task requires representing the surface in a continuous manner and providing an accurate estimate of the distance to the surface. In other words, the continuous representation of the surface corresponds to the interpolation between noisy measurements. In this section, we explore a few existing continuous and differentiable distance field approximations.

1) *Smooth-minimum*: A naive way to address the distance function estimation problem is to compute the distance between the query point  $\mathbf{x}$  and each of the surface observations  $\mathbf{x}_i$  and take the minimum of these distances. Unfortunately, the derivative of such an approach is not continuous. However, one can leverage the *smooth minimum* function defined as  $\frac{(\sum_{i=1}^Q \|\mathbf{x} - \mathbf{x}_i\| \exp(\lambda \|\mathbf{x} - \mathbf{x}_i\|))}{(\sum_{i=1}^Q \exp(\lambda \|\mathbf{x} - \mathbf{x}_i\|))}$ . This function is continuous and differentiable, which makes it suitable for its use in optimisation cost functions, but it does not account for any observation noise. Furthermore, as shown later in the experimental section of this paper, the smooth-minimum function does not interpolate the surface between the discrete observations.

2) *GPIS*: Originally the GPIS [15] represents the surface with the zero crossing of a GP-modelled scalar field. It is achieved by arbitrarily fixing the value of the surface observation to zero and adding positive and negative virtual observations inside and outside the closed surface. The interpolation abilities of GP regression allow GPIS to interpolate the surface between discrete measurements. In [26], with the use of linear operators [27] and observations of the normal vectors, the scalar field corresponds to the distance field close to the surface but converges to zero further away. It results in a scalar field that is not monotonic with respect to the true Euclidean distance to the surface. This is a significant drawback that prevents the use of GPIS for applications like scan registration or path planning.

3) *LogGPIS*: Motivated by heat-based methods [28], LogGPIS [16] models the space's heat at time  $t$  with a zero-mean GP scalar field  $v_t(\mathbf{x}) \sim \mathcal{GP}(0, k_v(\mathbf{x}, \mathbf{x}'))$  equal to one

on the surface. The inference of the GP model corresponds to the conduction of heat  $v$  in space after a short lapse of time  $t$  which is directly linked to the lengthscale of the kernel. According to Varadhan’s results [29], the limit  $\lim_{t \rightarrow 0} \{-\sqrt{t} \ln(v(\mathbf{x}, t))\}$  is equal to the distance from the surface. Using a fixed lengthscale and a specific kernel, the resulting distance field is the solution of a regularised version of the Eikonal equation. Unfortunately, this leads to a trade-off between accuracy and interpolation abilities: the limit in Varadhan’s equation requires a small lengthscale to approximate the true distance to the surface, but a small lengthscale removes the correlation between the GP observations, reducing the ability of the method to interpolate non-observed parts of the surface. Additionally, regardless of the kernel’s lengthscale, LogGPIS does not represent a truly Euclidean distance field of space. Considering the simple case of using only one observation  $\mathbf{x}_0$  of the surface and the Matérn 3/2 kernel, the heat is analytically expressed as  $v_t(\mathbf{x}) = (1 + \frac{\sqrt{3}d}{l}) \exp(-\frac{\sqrt{3}d}{l})$  with  $l$  the lengthscale of the kernel. Therefore, one can compute the error between the estimated distance and the ground truth as  $-\frac{l}{\sqrt{3}} \log(v_t(\mathbf{x})) - d = -\frac{l}{\sqrt{3}} \log(1 + \frac{\sqrt{3}d}{l})$ . The growth of the absolute error with respect to the distance depends to multi-observation scenarios as empirically shown later in our experiments.

### III. METHOD

Let us consider a set of points  $\mathbf{x}_i$  on the surface  $\mathcal{S}$  and a continuous scalar-valued field over  $\mathbb{R}^N$  that we refer to as the occupancy field  $o(\mathbf{x})$ . Arbitrarily, we set the observed value of the occupancy field to one at the locations  $\mathbf{x}_i \in \mathcal{S}$ . Note that this approach differs from the definitions of GPIS where the field is positive inside the object, negative outside, and the surface corresponds to the zero crossing of the field. By modelling the occupancy field with a GP

$$o(\mathbf{x}) \sim \mathcal{GP}(0, k_o(\mathbf{x}, \mathbf{x}')), \quad (6)$$

we can infer the occupancy at any point  $\mathbf{x} \in \mathbb{R}^N$  using (3):

$$\hat{o}(\mathbf{x}) = \mathbf{k}_o(\mathbf{x}, \mathbf{X}) (\mathbf{K}_o(\mathbf{X}, \mathbf{X}) + \sigma_o^2 \mathbf{I})^{-1} \mathbf{1}. \quad (7)$$

The value of the measurement’s uncertainty  $\sigma_o$  can be deduced from the noise on the position of the observations using a Taylor expansion of the kernel function [30]. By considering a monotonic, stationary, isotropic kernel with an infinite domain (i.e., a non-zero, distance-based kernel:  $k_o(\mathbf{x}, \mathbf{x}') \rightarrow k_o'(\|\mathbf{x} - \mathbf{x}'\|)$ ), let us define a *reverting* function  $r$  as

$$r(k_o(\mathbf{x}, \mathbf{x}')) = r(k_o'(\|\mathbf{x} - \mathbf{x}'\|)) \triangleq \|\mathbf{x} - \mathbf{x}'\|. \quad (8)$$

The proposed distance field consists in *reverting* the GP-inferred occupancy field<sup>1</sup> from (7) as  $\hat{d}(\mathbf{x}) = r(\hat{o}(\mathbf{x}))$ . Please note that the definition of the reverting function depends on the choice of the GP covariance kernel in (6). Examples of reverting functions will be provided later in this

<sup>1</sup>Please note that the GP inference is not explicitly upper-bounded. In our implementation, we are capping the occupancy to a maximum of 1.

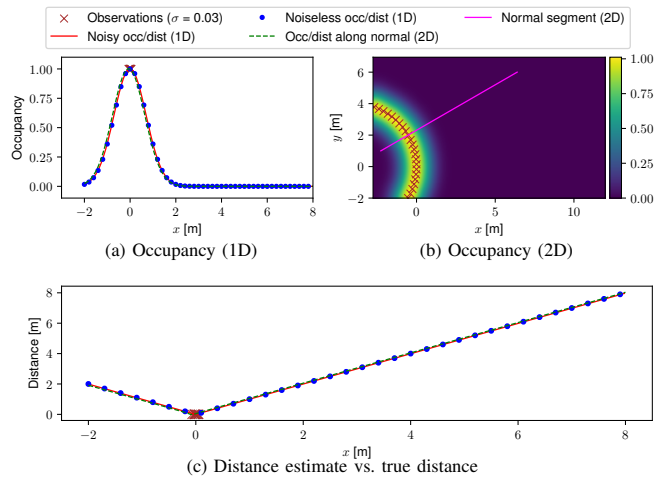


Fig. 2. Occupancy fields (1D and 2D) and distance estimates according to the *reverting* function. The plots (a) and (b) represent the GP occupancy inference (with Square Exponential kernel) using a set of noisy observations. The occupancy in (b) along the normal segment in fuchsia is also shown in (a). Plot (c) represents the corresponding distance estimates.

section. The variance of the estimate can be computed using (4) and propagating the uncertainty through the reverting function as  $\text{var}(\hat{d}) = \text{var}(\hat{o}) (\frac{\partial r(\hat{o})}{\partial \hat{o}})^2$ .

#### A. Motivation

Considering the simplistic one-noiseless-observation scenario already mentioned in Section II-B.3, it is easy to show from (7) and (8) that the reverting function provides the exact distance to the data point. Thanks to the probabilistic nature of GP regression, the occupancy field generated from multiple noisy observations of a point approximates well the ideal noiseless scenario as illustrated in Fig. 2 (a). By defining the distance field as  $r(\hat{o}(\mathbf{x}))$  we assume that the value of the occupancy field along the vectors normal to the surface can be faithfully approximated with the simplistic one-observation occupancy field as shown in Fig. 2.

#### B. Kernels, reverting functions, and hyper-parameters

Our method relies on the pair kernel/reverting function to estimate the distance field. This subsection discusses the case of the Rational Quadratic (RQ) kernel, the Square Exponential (SE) kernel, and the  $\nu = 3/2$  Matérn kernel. In their isometric form, these kernels depend on the Euclidean distance between the two input vectors. Using  $d = \|\mathbf{x} - \mathbf{x}'\|$ , Table I shows the different kernels as well as their reverting function (with  $\sigma^2$  as the scaling factor, and  $l$  the kernel’s lengthscale). In the case of the RQ and SE it is straightforward to find the reverting function with simple algebraic manipulations. Unfortunately, the  $\nu = 3/2$  Matérn kernel does not possess a known, closed-form reverting function. In this scenario, the reverting “function” can be formulated as a single-value non-linear optimisation problem.

All the kernels considered here depend on a scaling factor  $\sigma^2$  and a lengthscale  $l$ . While we arbitrarily fix  $\sigma = 1$ , the value of the lengthscale depends on the data at hand as it corresponds to the typical distance at which the data

	Covariance kernel ( $k_o(d)$ )	Reverting function ( $r(o)$ )
Rational quadratic	$\sigma^2 \left(1 + \frac{d^2}{2\alpha l^2}\right)^{-\alpha}$	$\sqrt{2\alpha l^2 \left(\left(\frac{o}{\sigma^2}\right)^{-\frac{1}{\alpha}} - 1\right)}$
Square exp.	$\sigma^2 \exp\left(-\frac{d^2}{2l^2}\right)$	$\sqrt{-2l^2 \log\left(\frac{o}{\sigma^2}\right)}$
Matérn $\nu = 3/2$	$\sigma^2 \left(1 + \frac{\sqrt{3}d}{l}\right) \exp\left(-\frac{\sqrt{3}d}{l}\right)$	$\operatorname{argmin}_d \ o - k_o(d)\ ^2$

TABLE I

COVARIANCE KERNELS AND ASSOCIATED REVERTING FUNCTIONS ( $B$  IS THE MODIFIED BESSEL FUNCTION OF THE SECOND KIND).

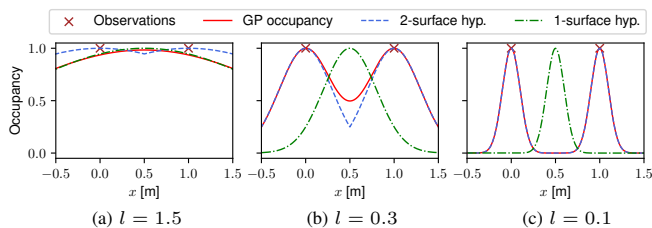


Fig. 3. Influence of the kernel’s lengthscale  $l$  on the occupancy field (1D example with SE kernel). Given two observations, a large  $l$  (a) interprets the data as noisy measurements of a single surface in the middle. A small  $l$  (c) corresponds to the hypothesis of two distinct surfaces.

points are correlated. Intuitively,  $l$  represents the “level of interpolation” as it characterises the “area of influence” of each of the observed points on the surface. In Fig. 3, we show the effect of varying the lengthscale for two non-collocated surface observations. The dashed lines correspond to the ideal occupancy values that lead to true distance through the reverting function for both the hypotheses of one surface in the middle (green) and two distinct surfaces (blue). One can see that with a large lengthscale  $l$ , the occupancy field interpolates between the data points. In that configuration, the data are interpreted as noisy measurements of a single surface located in the middle. With a small  $l$  value, the observations are decorrelated allowing for the distance to be calculated in that interval. In such a case, the data are interpreted as two distinct surfaces. Overall, while it is safe to define the lengthscale  $l$  empirically equal to one and a half times the typical distance between neighbour data points of the same surface, the choice of  $l$  is data dependent and will deserve more attention in future work (e.g., hyperparameter learning [31]).

### C. Advantages

In this subsection, we discuss how the proposed method addresses the drawbacks of existing methods mentioned in Section II-B. First, thanks to the interpolation properties of GP regression, the proposed method should outperform the naive smooth minimum approach when querying the distance field close to the surface. We empirically show it in Section V where queries on the surface between discrete observations lead to non-null distance estimates when using the smooth minimum approach. Regarding GPIS, the provided field is not a Euclidean field. Therefore, it cannot be used as a distance field over the full space  $\mathbb{R}^N$ .

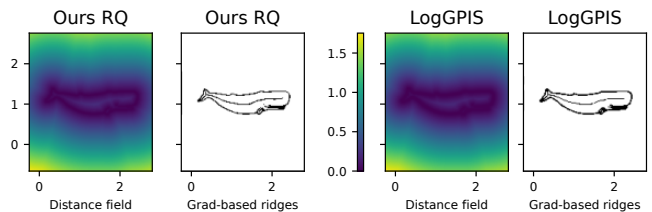


Fig. 4. Qualitative comparison of the proposed distance field and LogGPIS and their respective “ridges” (extracted with a threshold on the norm of the field’s gradient).

LogGPIS and the proposed method share a similar first step where the heat-diffusion/occupancy is inferred with GP regression. The main difference lies in the choice of the function operated over the GP-inferred value, and the constraints on the kernel and its hyperparameters. We have discussed in the previous subsection that the proposed method allows for the free selection of the kernel’s lengthscale to represent best the data at hand. On the other hand, LogGPIS suffers from a trade-off between accuracy and the ability to interpolate due to the limit in Varadhan’s results. Furthermore, we can establish a link between the proposed reverting function approach and LogGPIS with the  $\nu = 3/2$  Matérn kernel. Considering small distances  $d$ , one can approximate the kernel as

$$\lim_{d \rightarrow 0} \left(1 + \frac{\sqrt{3}d}{l}\right) \exp\left(-\frac{\sqrt{3}d}{l}\right) \approx \exp\left(-\frac{\sqrt{3}d}{l}\right). \quad (9)$$

Accordingly, this approximation would possess the following reverting function:  $\tilde{r}(o) = -\frac{l}{\sqrt{3}} \log(o)$ , corresponding to the logarithm operation over the GP-inferred value in LogGPIS. It is seemingly a close-range approximation of our method.

## IV. APPLICATIONS

As both LogGPIS [17] and the proposed method are using a monotonic function over a GP occupancy field, the resulting distance fields share some properties. As shown in Fig. 4, both methods’ distance fields have “ridges” in the same areas (ie., local extrema at the same locations). Thus, all the applications demonstrated in [17] (depth-camera odometry and mapping, path planning, surface reconstruction) can be performed with the proposed method. As an example, we released an open-source implementation of a depth-camera odometry pipeline based on the proposed distance field<sup>2</sup>. Due to the space limitation, we only present novel uses of GP-based distance fields such as echolocation and mapping with UGW sensing systems. Let us first introduce the UGW measurement model.

### A. Ultrasonic Guided Waves measurement model

Given a co-located emitter-receiver, at every measurement step  $i$ , a time signal  $s(t)$  is pulsed by the emitter to create an UGW that propagates radially around the emitter, *inside* the structure’s material. Simultaneously, the receiver collects the measurement  $z_i(t)$  that contains the ultrasonic echoes due

<sup>2</sup><https://github.com/UTS-CAS/gp-odometry>

to reflections of the excited wave on structural features (the boundaries  $\mathcal{S}$  of a metal panel in our case study). These measurements can be modelled by relying on the *image source* model, which states that the reception of any echo can be interpreted as a signal originating directly from a fictive image source (cf. Fig. 5(a)). The image sources' positions depend on the position of the actual emitter and the geometry of the surface  $\mathcal{S}$ . Considering isotropic material, the propagation is only a function of time and of the distance between the receiver and the image source resulting in the following measurement model:  $\tilde{z}_i(t) = \sum_{\rho \in \mathcal{I}(\mathbf{p}_i; \mathcal{S})} g(\|\rho - \mathbf{p}_i\|, t) * s(t) + n_i(t)$ , where  $\mathbf{p}_i$  is the emitter position,  $\mathcal{I}(\mathbf{p}_i; \mathcal{S})$  is the set of the image source positions for a surface  $\mathcal{S}$  and a real source position  $\mathbf{p}$ ,  $g(\|\rho - \mathbf{p}_i\|, t)$  is the acoustic transfer function of the propagation medium<sup>3</sup>,  $n(t)$  is an additive Gaussian noise term that we assume temporally and spatially white, and the symbol  $*$  denotes the convolution operation.

Let us generate a correlation signal between the measurement and the model to assess the likelihood that a *single* acoustic reflection occurred at any distance  $d$  from the emitter-receiver with:

$$z'_i(d) = \frac{\langle z_i(t), \hat{z}(d, t) \rangle}{\sqrt{\langle z_i(t), z_i(t) \rangle \langle \hat{z}(d, t), \hat{z}(d, t) \rangle}}, \quad (10)$$

where  $\hat{z}(d, t) = \hat{g}(2d, t) * s(t)$  is the expected signal containing an echo due to a reflection at a distance  $d$ , and  $\langle \cdot, \cdot \rangle$  denotes the usual scalar product for time-continuous signals. We subsequently retrieve the envelope of the correlation signals with  $e_i(d) = |z'_i(d) + j\mathcal{H}(z'_i(d))|$ , with  $\mathcal{H}$  denoting the Hilbert transform operator. The envelope signal ranges between 0 and 1, and it presents a local maximum in  $d$  if there is indeed a reflector at such distance, as illustrated in Fig. 5(b). The figure shows a distinguishable first echo at 0.08 m corresponding to the closest boundary and later echoes corresponding to the other edges of the plate.

To summarise, from a real measurement and the propagation model, the envelope signal allows us to assess the likelihood of a reflector being present at any distance  $d$ . Accordingly, considering the map (known or estimated) of the reflective features in the environment in the form of a point cloud and using the proposed GP-based distance field, it is possible to evaluate the envelope signal at any position in space to quantify the likelihood of a measurement being captured at such location.

### B. Echolocation

We aim at estimating the system's position  $\mathbf{p}_i$  by relying on ultrasonic measurements, noisy odometry information, and given the map (the plate boundaries  $\mathcal{S}$ ) in the form of a point cloud  $\mathbf{X}$  using a particle filter as in [33]. Such filters usually provide satisfactory solutions to the localisation problem when the dynamic and observation models are non-linear, and the process and measurement noises are non-Gaussian [34], as in our case study. Yet, the method described

<sup>3</sup>A standard propagation model for an UGW propagating in a metal panel is  $\hat{g}(r, \omega) \approx e^{-jk(\omega)r} / \sqrt{k(\omega)r}$ , where  $k(\omega)$  is the wavenumber of the major acoustic mode. More details can be found in [32].

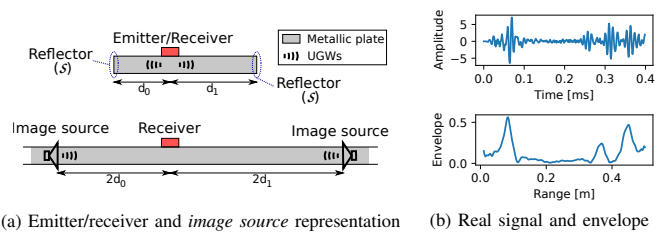


Fig. 5. Illustration of the emitter/receiver setup and the equivalent *image source* representation when considering only first-order echoes (a), and example of an acoustic measurement acquired on an aluminium plate with the corresponding envelope signal (b).

in [33] can only be applied to metal panels with a rectangular shape. Hence, we propose a modification to the calculation of the particles' weights to make the approach applicable to arbitrary surface geometries, using the proposed GP-based distance field.

The localisation approach relies on the aforementioned envelope signals  $e_i(d)$  to determine the likelihood of each measurement and update the weights  $w_i^n$  of the particles as follows:

$$w_i^n = \eta \exp\left(\beta e_i(\hat{d}(\mathbf{p}_i^n))\right) w_{i-1}^n, \quad (11)$$

where  $\hat{d}(\mathbf{p}_i^n)$  is the GP-based distance of the  $n$ -th particle to the closest point on the surface  $\mathcal{S}$  computed with (7) and the reverting function (8),  $\eta$  is the normalization factor, and  $\beta$  is a positive parameter. The filtering process consists of the succession of motion and measurement updates with regular resampling of the particles after a fixed number of steps (5 in our experiments). The filter's output corresponds to the mean coordinates of the 25% best particles (highest weights).

### C. Mapping

For the purpose of mapping, the goal is to estimate the continuous distance field given the system's localisation and the UGW measurements. While the UGW measurements contain information about the distance to the closest surface (peaks in the envelope  $e_i(d)$ ), this scenario is different from the depth-camera/lidar mapping of [17] as there is no bearing information available.

Similarly to the echolocation scenario, we use the envelope signals  $e_i(d)$  as proxies to quantify the likelihood of the measurements given the state variables. In the context of echolocation, the map points  $\mathbf{X}$  are known and the measurement positions  $\mathbf{p}_i$  are estimated whereas for mapping it is the opposite: the sensing positions  $\mathbf{p}_i$  are known and the state variables consist of a set of virtual observations  $\mathbf{X}$  of the map (same  $\mathbf{X}$  as in the GP formulation in (7)). The maximisation of the envelope measurements is formulated as a non-linear least-square optimisation problem

$$\arg\min_{\mathbf{X}} \left( \sum_{i=1}^N \|1 - e_i(\hat{d}(\mathbf{p}_i, \mathbf{X}))\|^2 + \alpha \sum_{i=2}^Q \|\mathbf{x}_i - \mathbf{x}_{i-1}\|^2 \right), \quad (12)$$

Method	RMSE [m] close-range	RMSE [m] far-range	Coverage ratio
LogGPIS	0.0133	0.0689	1.0
Smooth min	0.0194	<u>0.0166</u>	1.0
Ours SE	<b>0.0083</b>	<b>0.0105</b>	0.3245
Ours Matern 3/2	0.0092	0.0279	1.0
Ours RQ	<u>0.0085</u>	0.0185	1.0

TABLE II  
AVERAGE RMSE 100 DIFFERENT SIMULATED ENVIRONMENTS (40K  
SAMPLES EACH)

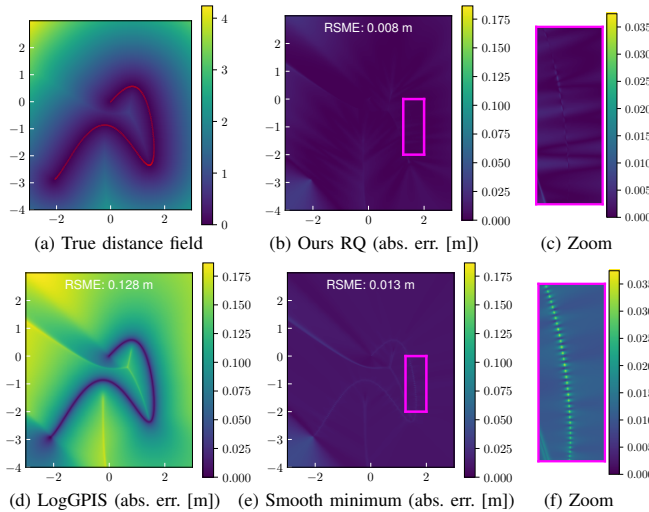


Fig. 6. Accuracy comparison of the proposed distance field, LogGPIS [16], and the smooth minimum function. The surface samples and the true distance field are shown in red in (a). The absolute error between the ground truth and the estimated fields are shown in (b), (d) and (e), while (c) and (f) correspond to zoom-ins on the fuchsia area in (b) and (e) (with an adjusted colourmap).

with  $\alpha \sum_{i=2}^Q \|\mathbf{x}_i - \mathbf{x}_{i-1}\|^2$  a naive regularisation term to prevent under-constrained state variables in case virtual observation estimates are located in non-observed areas. While being conceptually simple, solving (12) is not an easy task due to the many extrema present in the envelope signals (c.f. Fig 5(b)). To provide a decent initial guess, we perform the mapping method considering only a single peak in each envelope signal by detecting the distances  $d_i$  of the peaks corresponding to the first echoes:

$$\operatorname{argmin}_{\mathbf{X}} \left( \sum_{i=1}^N \|d_i - \hat{d}(\mathbf{p}_i, \mathbf{X})\|^2 + \alpha \sum_{i=2}^Q \|\mathbf{x}_i - \mathbf{x}_{i-1}\|^2 \right). \quad (13)$$

Solving for (13) and then (12) with the Trust Region Reflective algorithm allows for the estimation of the virtual observations therefore of the continuous occupancy field  $\hat{o}$  and the associated distance field  $\hat{d}$ .

## V. EXPERIMENTS

### A. Distance field

In this subsection, we benchmark the proposed method against LogGPIS [16] and the simple smooth minimum func-

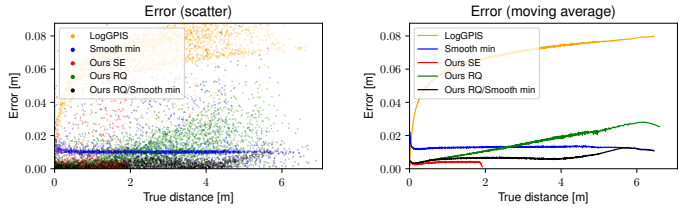


Fig. 7. Comparison of the error distribution between LogGPIS [16], the smooth minimum function, and the proposed method with the RQ and SE kernels (2500 random samples among 100 simulated environments).

tion presented in Section II-B.1 (with  $\lambda = -50$ ) over 100 simulated 2D environments. Each environment is generated using the sum of sine functions with both random amplitudes and frequencies. To evaluate the different methods, we query 40k distance measurements per environment following a regular grid and compute the Root Mean Squared Error (RMSE) against the ground truth. Table II reports the average RMSE for each method considering separately close-range (under 0.05 m) and far-range (above 0.05 m) from the surface. The last column corresponds to the success rate of each method. Failure cases correspond to inferences of the occupancy field that are inferior to machine precision, leading to singularities in the reverting function (with SE kernel:  $\log(0) = \text{NaN}$ ).

Overall, our method consistently outperforms the other methods at close range. Especially, one can see the high error of the smooth minimum corresponding to its inability to interpolate between the observations. One occurrence of the simulated data is shown in Fig. 6. The zoomed-in plots clearly illustrate the lack of interpolation ability of the smooth minimum approach. Further away from the surface, the accuracy of the smooth minimum is on par with the proposed method. In Fig. 7 we display the absolute error of 2500 inferences randomly selected among the query points aforementioned. Smoothing the plot with a moving average one can see the error of the LogGPIS following a  $\log(1+x)$  curve as predicted in Section II-B.3. Fig. 6 also introduces a merged approach combining the proposed method and the smooth minimum function leveraging the best of both methods: trusting the GP reverting approach close to the surface and the smooth minimum further away with a smooth transition in between. Note that the smooth minimum tends to overestimate (positive error) the distance while ours tends to underestimate it (negative error). Accordingly, the fusion of our approach and the smooth minimum leads to better accuracy than the two methods independently.

### B. Echolocation

In this subsection, we evaluate the proposed echolocation algorithm based on our GP distance field (with RQ kernel and  $\alpha = 100$ ). We have collected UGW measurements in an aluminium metal panel with dimensions 600x450x6mm. The experimental setup consists of an emitter/receiver pair of nearly collocated transducers (as shown in Fig. 1) placed by hand on the vertices of a 9x12 regular grid whose positions are carefully recorded. For every position, the UGW is generated using a two-tone burst sinusoidal wave at

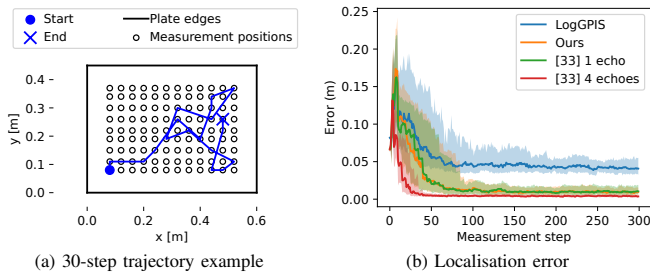


Fig. 8. Real-world localisation experiments. (a) illustrates the trajectories generation from a fixed grid of UGW measurements. (b) shows the median error obtained with several methods over 100 trajectories (the transparent areas correspond to the spread of the error between the 25<sup>th</sup> and 75<sup>th</sup> percentiles).

100 kHz (excitation signal  $s(t)$ ) while the receiver collects the ultrasonic response. In total, 108 measurements were acquired. From these grid-based measurements, we generated 100 trajectories of 300 steps by randomly navigation through the grid. Fig. 8(a) illustrates 30 steps of such a trajectory.

We benchmark the localisation accuracy of the following methods: the particle filter with LogGPIS, the particle filter with our novel reverting-function distance field, and the method from [33]. In [33], the environment is modelled with a set of geometric primitives (4 lines for our rectangular plate) and a particle filter is also used for localisation. The parametric map approach allows for the computation of multiple echoes as part of the measurement model of each particle while our approach only considers the first echo. For a more thorough comparison, we also implemented a version of [33] that considers solely the closest edge for each particle. Note that it corresponds to the particle filter described in this work using the ground truth distance field of the rectangular panel. We denote the two versions as [33] 1 echo and [33] 4 echoes.

Fig. 8(b) shows the median error as a function of the measurement step for the 100 trajectories. The fact that [33] 1 echo and *Ours* result in very similar accuracy supports the evidence that the proposed representation approximates well the true Euclidean distance field. It is not the case for LogGPIS which limits the overall system’s performance in accordance with our simulated experiments in Section V-A. While providing satisfying levels of accuracy ( $\approx 0.01$  m), our method does not perform as well as [33] 4 echoes. This demonstrates the importance of considering multiple echoes to improve the system’s performance. Future work will explore the integration of multiple echoes in our GP representation.

### C. Mapping

To evaluate our UGW-based mapping approach, we use the 108 measurements presented in the previous setup as input. In Fig. 9, we show the different mapping results using LogGPIS, the proposed distance field (denoted *ours*), and Delay-and-Sum (DaS) beamforming. The former is a non-parametric approach for acoustic reflector mapping that assess the likelihood of the presence of a reflector at any

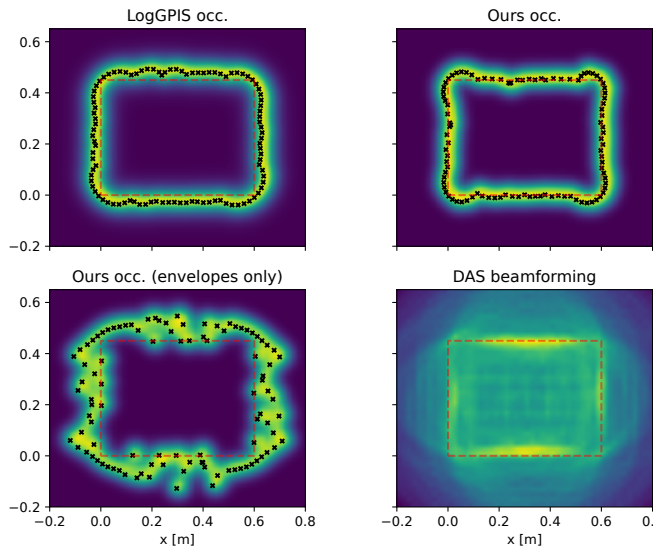


Fig. 9. Occupancy field/reflector likelihood estimation for UGW-based mapping. The dashed line represents the ground truth of the metal panel’s edges, and the crosses correspond to the optimised virtual observations  $\mathbf{X}$ .

position  $\mathbf{x}$  by summing the values of each envelope signal  $e_i$  as  $\mathcal{L}(\mathbf{x}) = \sum_{i=1}^N e_i(\|\mathbf{x}_i - \mathbf{x}\|)$ . Note that the DaS approach provides information about the likelihood of a reflector being present at a given location whereas the other methods provide clear occupancy fields that can be directly interpreted as distance fields ([17] and proposed method) for robotic applications down the line like localisation or path planning. Accordingly, the beamforming-generated map needs additional complex processing to allow its use in autonomous systems.

To provide the reader with additional insight into our mapping pipeline, we run the mapping experiment without the first distance-based optimisation step (13) (denoted *Ours* (*distance-only*) in Fig. 9). One can see that even if some estimated observations are present at the location of the plate’s edges, the problem does not converge to the global minimum. Converting the occupancy fields into distance fields and analysing the results inside the plate, we obtain distance RMSEs of 0.021 m for mapping using LogGPIS’ distance field, 0.016 m with *Ours* (*envelope-only*), and 0.006 m with *Ours*. These results demonstrate the ability of our novel GP-based distance to represent accurately the environment in a non-parametric manner while providing readily available information (occupancy and distance to obstacle) for later use of the mapping results.

## VI. CONCLUSION

In this paper, we presented a novel GP-based distance field estimation method. Using a point cloud as input, the proposed method first infers an occupancy value based on standard GP regression before applying a kernel reverting function. We empirically show that our approach significantly outperforms state-of-the-art representations with higher levels of accuracy allowing for novel applications

which rely on precise Euclidean distance functions. Accordingly, this work presents frameworks for echolocation and mapping using UGWs. With real-world experiments, we demonstrated similar levels of localisation accuracy as those of parametric-based representations. In the mapping context, our method does provide useful maps for various robotics applications (like localisation or path planning) while traditional DaS maps need further processing. Future work will explore the use of multi echoes in our GP model to improve the UGW echolocation and mapping frameworks in terms of robustness and accuracy.

#### REFERENCES

- [1] C. Cadena, L. Carlone, H. Carrillo, Y. Latif, D. Scaramuzza, J. Neira, I. Reid, and J. J. Leonard, "Past, present, and future of simultaneous localization and mapping: Toward the robust-perception age," *IEEE Transactions on Robotics*, vol. 32, no. 6, pp. 1309–1332, 2016.
- [2] R. Mur-Artal and J. D. Tardós, "ORB-SLAM2: an open-source SLAM system for monocular, stereo, and RGB-D cameras," *IEEE Transactions on Robotics (T-RO)*, vol. 33, no. 5, pp. 1255–1262, 2017.
- [3] A. Elfes, "Using occupancy grids for mobile robot perception and navigation," *Computer*, vol. 22, no. 6, pp. 46–57, 1989.
- [4] A. Hornung, K. M. Wurm, M. Bennewitz, C. Stachniss, and W. Burgard, "Octomap: an efficient probabilistic 3d mapping framework based on octrees," *Autonomous Robots*, pp. 189–206, 2013.
- [5] E. G. Tsardoulis, A. Iliakopoulou, A. Kargakos, and L. Petrou, "A review of global path planning methods for occupancy grid maps regardless of obstacle density," *Int. J. of Rob. Res.(IJRR)*, 2016.
- [6] S. Izadi, D. Kim, O. Hilliges, D. Molyneaux, R. Newcombe, P. Kohli, J. Shotton, S. Hodges, D. Freeman, A. Davison, et al., "Kinectfusion: real-time 3d reconstruction and interaction using a moving depth camera," in *Proc. of the ACM symposium*, 2011, pp. 559–568.
- [7] H. Oleynikova, A. Millane, Z. Taylor, E. Galceran, J. Nieto, and R. Siegwart, "Signed distance fields: A natural representation for both mapping and planning," in *RSS 2016 Workshop: Geometry and Beyond-Representations, Physics, and Scene Understanding for Robotics*, 2016.
- [8] H. Oleynikova, Z. Taylor, M. Fehr, R. Siegwart, and J. Nieto, "Voxblox: Incremental 3d euclidean signed distance fields for on-board mav planning," in *2017 IEEE/RSJ International Conference on Intelligent Robots and Systems (IROS)*, 2017, pp. 1366–1373.
- [9] L. Han, F. Gao, B. Zhou, and S. Shen, "Fiesta: Fast incremental euclidean distance fields for online motion planning of aerial robots," in *2019 IEEE/RSJ International Conference on Intelligent Robots and Systems (IROS)*. IEEE, 2019, pp. 4423–4430.
- [10] J. Ortiz, A. Clegg, J. Dong, E. Sucar, D. Novotny, M. Zollhoefer, and M. Mukadam, "isdf: Real-time neural signed distance fields for robot perception," *arXiv preprint arXiv:2204.02296*, 2022.
- [11] E. Sucar, S. Liu, J. Ortiz, and A. J. Davison, "imap: Implicit mapping and positioning in real-time," in *Proceedings of the IEEE/CVF International Conference on Computer Vision*, 2021, pp. 6229–6238.
- [12] Z. Zhu, S. Peng, V. Larsson, W. Xu, H. Bao, Z. Cui, M. R. Oswald, and M. Pollefeys, "Nice-slam: Neural implicit scalable encoding for slam," in *Proceedings of the IEEE/CVF Conference on Computer Vision and Pattern Recognition*, 2022, pp. 12 786–12 796.
- [13] D. Driess, J.-S. Ha, M. Toussaint, and R. Tedrake, "Learning models as functionals of signed-distance fields for manipulation planning," in *Conference on Robot Learning*. PMLR, 2022, pp. 245–255.
- [14] M. Pantic, C. Cadena, R. Siegwart, and L. Ott, "Sampling-free obstacle gradients and reactive planning in neural radiance fields (nerf)," *arXiv preprint arXiv:2205.01389*, 2022.
- [15] O. Williams and A. Fitzgibbon, "Gaussian process implicit surfaces," 2007.
- [16] L. Wu, K. M. B. Lee, L. Liu, and T. Vidal-Calleja, "Faithful euclidean distance field from log-gaussian process implicit surfaces," *IEEE Robotics and Automation Letters*, vol. 6, no. 2, pp. 2461–2468, 2021.
- [17] L. Wu, K. M. B. Lee, C. Le Gentil, and T. Vidal-Calleja, "Log-gpismop: A unified representation for mapping, odometry, and planning," *IEEE Transactions on Robotics*, pp. 1–17, 2023.
- [18] J.-P. A. Ivan, T. Stoyanov, and J. A. Stork, "Online distance field priors for gaussian process implicit surfaces," *IEEE Robotics and Automation Letters*, vol. 7, no. 4, pp. 8996–9003, 2022.
- [19] S. T. O'Callaghan and F. T. Ramos, "Gaussian process occupancy maps," *The International Journal of Robotics Research*, vol. 31, no. 1, pp. 42–62, 2012.
- [20] I. Dokmanić, L. Daudet, and M. Vetterli, "From acoustic room reconstruction to slam," in *2016 IEEE International Conference on Acoustics, Speech and Signal Processing (ICASSP)*. Ieee, 2016, pp. 6345–6349.
- [21] M. Kreković, I. Dokmanić, and M. Vetterli, "Echoslam: Simultaneous localization and mapping with acoustic echoes," in *2016 IEEE International Conference on Acoustics, Speech and Signal Processing (ICASSP)*. Ieee, 2016, pp. 11–15.
- [22] D. Ribas, P. Ridao, J. D. Tardós, and J. Neira, "Underwater slam in a marina environment," in *2007 IEEE/RSJ International Conference on Intelligent Robots and Systems*. IEEE, 2007, pp. 1455–1460.
- [23] M. Y. Cheung, D. Fourie, N. R. Rypkema, P. V. Teixeira, H. Schmidt, and J. Leonard, "Non-gaussian slam utilizing synthetic aperture sonar," in *2019 International Conference on Robotics and Automation (ICRA)*. IEEE, 2019, pp. 3457–3463.
- [24] R. Worley, Y. Yu, and S. Anderson, "Acoustic echo-localization for pipe inspection robots," in *2020 IEEE International Conference on Multisensor Fusion and Integration for Intelligent Systems (MFI)*. IEEE, 2020, pp. 160–165.
- [25] O. L. Ouabi, P. Pomarede, M. Geist, N. F. Declercq, and C. Pradalier, "A FastSLAM Approach Integrating Beamforming Maps for Ultrasound-Based Robotic Inspection of Metal Structures," *IEEE Robotics and Automation Letters*, vol. 6, no. 2, pp. 2908–2913, 2021.
- [26] W. Martens, Y. Poffet, P. R. Soria, R. Fitch, and S. Sukkarieh, "Geometric priors for gaussian process implicit surfaces," *IEEE Robotics and Automation Letters*, vol. 2, no. 2, pp. 373–380, 2017.
- [27] S. Särkkä, "Linear operators and stochastic partial differential equations in Gaussian process regression," *Artificial Neural Networks and Machine Learning–ICANN 2011*, pp. 151–158, 2011.
- [28] K. Crane, C. Weischedel, and M. Wardetzky, "Geodesics in heat: A new approach to computing distance based on heat flow," *ACM Transactions on Graphics (TOG)*, vol. 32, no. 5, October 2013.
- [29] S. R. S. Varadhan, "On the behavior of the fundamental solution of the heat equation with variable coefficients," *Communications on Pure and Applied Mathematics*, vol. 20, pp. 431–455, 1967.
- [30] A. McHutchon and C. E. Rasmussen, "Gaussian process training with input noise," in *Proceedings of the 24th International Conference on Neural Information Processing Systems*, ser. NIPS'11. Red Hook, NY, USA: Curran Associates Inc., 2011, p. 1341–1349.
- [31] C. E. Rasmussen and C. K. I. Williams, *Gaussian Processes for Machine Learning*. The MIT Press, 2006.
- [32] Z. Su and L. Ye, *Identification of Damage Using Lamb Waves: From Fundamentals to Applications*, 01 2009, vol. 48.
- [33] O.-L. Ouabi, P. Pomarede, M. Geist, N. F. Declercq, and C. Pradalier, "Monte-carlo localization on metal plates based on ultrasonic guided waves," in *International Symposium on Experimental Robotics*. Springer, 2021, pp. 345–353.
- [34] S. Thrun, W. Burgard, D. Fox, et al., *Probabilistic robotics*, vol. 1. MIT press Cambridge, 2005.